

Article

Synthesis and Characterization of Graphite Intercalation Compounds with Sulfuric Acid

Gintare Rimkute ^{1,*}, Mantvydas Gudaitis ², Jurgis Barkauskas ¹, Aleksej Zarkov ^{1,*}, Gediminas Niaura ² and Justina Gaidukevic ¹

¹ Institute of Chemistry, Faculty of Chemistry and Geosciences, Vilnius University, Naugarduko Str. 24, LT-03225 Vilnius, Lithuania; jurgis.barkauskas@chf.vu.lt (J.B.); justina.gaidukevic@chf.vu.lt (J.G.)

² Department of Organic Chemistry, Center for Physical Sciences and Technology (FTMC), Saulėtekio Av. 3, LT-10257 Vilnius, Lithuania; mantvydas.gudaitis@chgf.stud.vu.lt (M.G.); gediminas.niaura@ftmc.lt (G.N.)

* Correspondence: gintare.rimkute@chgf.vu.lt (G.R.); aleksej.zarkov@chf.vu.lt (A.Z.)

Abstract: In this work, graphite intercalation compounds (GICs) were synthesized using three different oxidizers: $(\text{NH}_4)_2\text{S}_2\text{O}_8$, $\text{K}_2\text{S}_2\text{O}_8$, and CrO_3 with and without P_2O_5 as a water-binding agent. Furthermore, the samples obtained were heat-treated at 800 °C. Specimens were characterized by optical microscopy, Raman spectroscopy, Fourier transform infrared spectroscopy (FTIR), X-ray powder diffraction (XRD), and scanning electron microscopy (SEM). The correlation between different characteristic parameters of the Raman analysis has shown that the use of CrO_3 results in a much higher structural disorder compared to the products obtained using persulfate oxidizers. Narrowing the correlation set revealed that minimal defect concentration can be reached by using $\text{K}_2\text{S}_2\text{O}_8$, while the use of $(\text{NH}_4)_2\text{S}_2\text{O}_8$ causes a slightly higher concentration of defects. It was also established that the additional use of P_2O_5 can help to achieve more effective intercalation and has a positive effect on the formation of the stage I GIC phase. After heat treatment, the intercalated products mostly return to a graphite-like structure; however, the samples obtained with CrO_3 stand out with the most significant changes in their surface morphology. Therefore, analysis suggests that GICs obtained using persulfate oxidizers and P_2O_5 could be a candidate to produce high-quality graphene or graphene oxide.

Keywords: graphite intercalation compounds; graphite bisulfate; staging in graphite intercalation compounds; structural characterization; thermal treatment



Citation: Rimkute, G.; Gudaitis, M.; Barkauskas, J.; Zarkov, A.; Niaura, G.; Gaidukevic, J. Synthesis and Characterization of Graphite Intercalation Compounds with Sulfuric Acid. *Crystals* **2022**, *12*, 421. <https://doi.org/10.3390/cryst12030421>

Academic Editor: Sawanta S. Mali

Received: 3 March 2022

Accepted: 16 March 2022

Published: 18 March 2022

Publisher's Note: MDPI stays neutral with regard to jurisdictional claims in published maps and institutional affiliations.



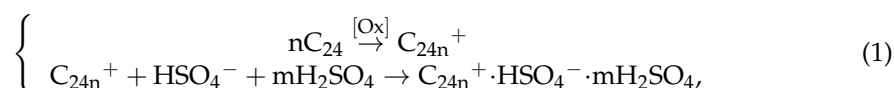
Copyright: © 2022 by the authors. Licensee MDPI, Basel, Switzerland. This article is an open access article distributed under the terms and conditions of the Creative Commons Attribution (CC BY) license (<https://creativecommons.org/licenses/by/4.0/>).

1. Introduction

A special group of compounds known as graphite intercalation compounds (GICs) was first mentioned in 1840 by German chemist C. Schafhaeutl [1]. In 1855, B. C. Brodie described the synthesis of GIC using a mixture of sulfuric and nitric acids [2]. This work is considered to be the beginning of GIC research. Nowadays, research in the area of GICs is the focus, especially due to their use in Li-ion batteries [3]. Furthermore, GICs can form numerous groups of compounds. A variety of GICs can be generally divided into two groups: covalent and ionic. The number of compounds in the latter group far exceeds that in the former [4]. Ionic GICs, such as graphite salts, graphite-halogen compounds, graphite-metal chloride compounds, and graphite alkali-metal compounds, have received more recognition than covalent GICs due to the change in the electronic properties of graphite, which is attributed to the π -bonds that can donate or accept electrons [5]. Therefore, ionic GICs can be further divided into donor-type (Lewis base guests, e.g., alkali metals) and acceptor-type (Lewis acid guests, e.g., strong mineral acids), while unique redox amphoteric characteristics enable graphite to host both cations and anions.

The significance of GICs is not limited to their use in energy storage systems. Some of them reveal the superconductivity phenomenon at low temperatures, while others are used

as reagents and catalysts in organic synthesis [6,7]. Another relevant area where GICs play a key role is the production of graphene and graphene oxide. High-quality, low-defective graphene can be obtained using the GIC as a direct precursor [8]. Likewise, GIC, known as graphite bisulfate (GBS), forms as an intermediate in the process of the preparation of graphene oxide, which is widely used for the further production and processing of graphene [9]. GBS is the GIC, where graphite layers are intercalated by HSO_4^- ions and H_2SO_4 molecules. The reaction of GBS formation implies oxidation of the graphite matrix conjugated with insertion of the molecules and ions in the presence of an oxidant (Ox):



where m/n ratio stands for the staging index, i.e., the number of graphite layers between two intercalant layers [10]. Formula $\text{C}_{24}^+ \cdot \text{HSO}_4^- \cdot 2\text{H}_2\text{SO}_4$ represents the stage I compound, where a single layer of graphene is alternated regularly with intercalated species. In subsequent stages (stage II, stage III, etc.), the corresponding number of graphene layers (2, 3, etc.) are separated by layers of HSO_4^- ions and H_2SO_4 molecules [11].

GBS is also the most widely used precursor for manufacturing exfoliated graphite, which is valued for compactness, flexibility, high electrical and thermal conductivity, and corrosion resistance. For this purpose, GBS is treated with microwaves or thermal shock conditions. Under these conditions, graphene layers are separated and form a characteristic cellular structure. When pressed without binder, exfoliated graphite can be formed into disks, coatings, fabric, etc., and used as a fire retardant, absorbent, electrode material, photo-catalyst, and many similar cases [12].

Although GICs have been known for a long time and are extensively used nowadays, the knowledge in this field so far is not sufficient. Thermodynamics of GIC formation do not always correspond to the theoretical model, and it is still difficult to predict the potential of the system that includes GIC. Simultaneously, very limited structural information is given in the literature concerning these systems, at most due to their instability. Since the properties of GIC with the same chemical composition may vary depending on graphite precursor, preparation conditions, and other factors, it is important to investigate as many different synthesis variations as possible [13].

In this research, GBS compounds were chemically synthesized using three different oxidizing agents as well as P_2O_5 as a water binding agent. All obtained samples were heat-treated at 800°C in order to get exfoliated graphite. The obtained samples were investigated using optical microscopy, Raman spectroscopy, Fourier transform infrared spectroscopy (FTIR), X-ray powder diffraction (XRD), and scanning electron microscopy (SEM).

2. Materials and Methods

2.1. Materials

In the synthesis, all reagents were used without further purification. Extra pure graphite powder ($<50\ \mu\text{m}$ ($\geq 99.5\%$)) was purchased from Merck KGaA (Darmstadt, Germany), H_2SO_4 (98%), $(\text{NH}_4)_2\text{S}_2\text{O}_8$ (98%), $\text{K}_2\text{S}_2\text{O}_8$ (99.99%), CrO_3 (99.99%), and P_2O_5 (99%)—from Sigma-Aldrich (Darmstadt, Germany).

2.2. Synthesis of GBS Products

The synthesis of GBS was performed according to the protocol described by Dimiev et al. [14]. Three different oxidizing agents (ammonium persulfate— $(\text{NH}_4)_2\text{S}_2\text{O}_8$, potassium persulfate— $\text{K}_2\text{S}_2\text{O}_8$, and chromium trioxide— CrO_3) were used. The oxidizing mixture was prepared in a 50 mL Erlenmeyer flask with a ground glass joint by adding 1.6 g of an oxidant to 10 mL of H_2SO_4 ($\geq 98\%$) at constant swirling. After 5 min, 0.25 g of graphite powder was slowly added to the solution of the oxidizing mixture. The Erlenmeyer flask was covered with a ground glass stopper, and the swirling procedure was continued for 1 week. The procedure of GBS synthesis was repeated with all three oxidizing agents,

adding 2 g of P_2O_5 to the oxidizing mixture. Abbreviations of obtained 6 GBS products are summarized in Table 1. Additional synthesis in the mixture of CrO_3 and H_2SO_4 was repeated following the protocol, but at the end stage, 40 mL of deionized water was added, ensuring that the temperature of the mixture would not rise above 60 °C. The GBS product of this synthesis is also introduced in Table 1. After synthesis, the GBS products were filtered through a sintered glass filter and stored in a desiccator.

Table 1. Synthesized and heat-treated GBS products.

Oxidizer	Addition of P_2O_5	Addition of H_2O	Thermal Treatment	Abbreviation in Text
$(NH_4)_2S_2O_8$	—	—	—	A000
$K_2S_2O_8$	—	—	—	P000
CrO_3	—	—	—	C000
$(NH_4)_2S_2O_8$	+	—	—	A100
$K_2S_2O_8$	+	—	—	P100
CrO_3	+	—	—	C100
CrO_3	—	+	—	C010
$(NH_4)_2S_2O_8$	—	—	+	A001
$K_2S_2O_8$	—	—	+	P001
CrO_3	—	—	+	C001
$(NH_4)_2S_2O_8$	+	—	+	A101
$K_2S_2O_8$	+	—	+	P101
CrO_3	+	—	+	C101
CrO_3	—	+	+	C011

All GBS samples obtained by the synthesis described above were heat-treated under thermal shock conditions. For this purpose, samples were placed into ceramic combustion boats, which were inserted into a quartz glass tube. The tube was sealed and placed in a furnace preheated to 800 °C (heating rate was 5 °C·min⁻¹) and annealed in argon ambient for 15 min. The flow rate of argon was maintained at 15 mL·min⁻¹. Samples reached 800 °C approximately in a minute. After a set time, the tube was taken out of the furnace and cooled to room temperature in 15 min (cooling rate was about 50 °C·min⁻¹). The heat-treated samples were stored in a desiccator. The thermally treated products are summarized in Table 1. In the table, “+” means that the P_2O_5 or H_2O was added to the reaction mixture or that the obtained products were thermally treated.

2.3. Characterization

Optical images were obtained using a BX51, Olympus optical microscope (Tokyo, Japan) at a magnification of 50×. Raman spectra were recorded using an inVia, Renishaw spectrometer (Wotton-under Edge, UK) equipped with an optical microscope at a magnification of 20× and an objective numerical aperture of 0.40, a CCD camera, and 1800 grooves·mm⁻¹ grating. The laser excitation wavelength was 532 nm, beam concentration area—2 μm², and integration time—100 s. To analyze the band changes, Raman peaks were fitted with a pseudo-Voigt function—a linear combination of Lorentzian and Gaussian functions [15]. FTIR measurements were carried out using a Frontier PerkinElmer FTIR spectrometer (Seattle, WA, USA) in the spectral range of 4000–800 cm⁻¹ with 4 cm⁻¹ resolution and 25 scans. The samples were prepared using the KBr pellet technique. For this purpose, sample powder (0.5% by wt.) was mixed with pure KBr powder. Then, for 5 min, the mixtures were pressed into transparent pellets using a CrushIR PIKE hydraulic press (Madison, WI, USA) with 8 ton·cm⁻² pressure. Background correction was made using a reference blank KBr pellet. The wet samples were analyzed by applying a thin layer of the substance on the surface of a pure KBr pellet. XRD measurements were performed in the 2θ range between 5–60° with a Miniflex II, Rigaku diffractometer (Neu-Isenburg,

Germany) (Cu K α radiation with a graphite monochromator). The interlayer distance d was calculated according to Bragg's equation [16]:

$$n\lambda = 2d \cdot \sin \theta, \quad (2)$$

where n is a positive integer, λ is the wavelength of the X-ray, d is the interlayer distance and θ is the scattering angle. Crystallite size L was calculated using the Scherrer equation [17]:

$$L = \frac{0.89 \cdot \lambda}{\beta \cdot \cos \theta}, \quad (3)$$

where λ is the wavelength of the X-ray, β is a full width at half maximum (FWHM) and θ is the scattering angle. The morphology of the samples was examined using a SU-70, Hitachi microscope (Tokyo, Japan) at an accelerating voltage of 10 kV and magnification of 5000 \times .

3. Results and Discussion

Synthesized and heat-treated GBS products were characterized using optical and SEM microscopy, FTIR and Raman spectroscopy, and XRD measurements. GBS products are unstable (sensitive to moisture and higher temperatures) and have a significant corrosive effect. For this reason, SEM and XRD analyses were applied only to those products (treated at higher temperatures or washed with H $_2$ O), from which the H $_2$ SO $_4$ intercalant was removed.

The effect of the synthesis duration of GBS products was examined using optical microscopy. The specimens for analysis were collected after 2 h and 24 h from the beginning of the synthesis, respectively. The optical micrographs of the GBS samples are presented in Figures 1 and 2.

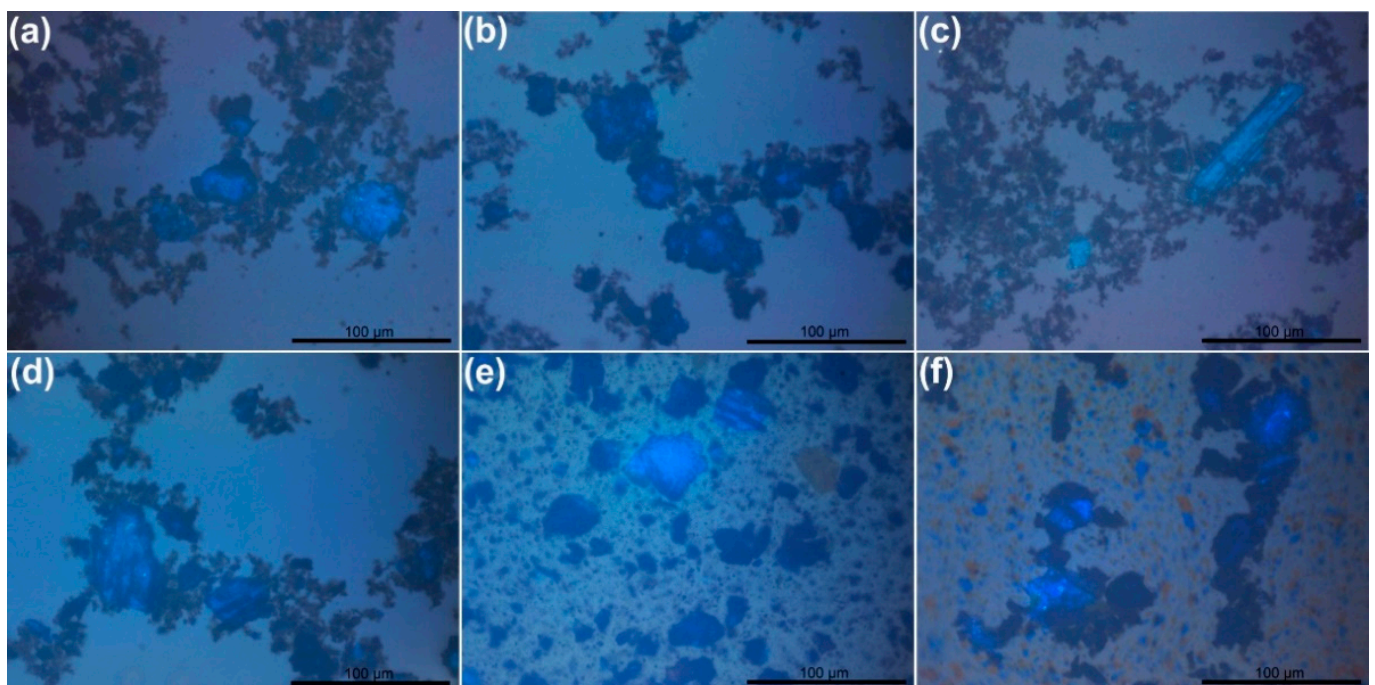


Figure 1. Optical micrographs of GBS obtained after 2 h from the start of the synthesis—A000 (a), A100 (b), P000 (c), P100 (d), C000 (e), and C100 (f).

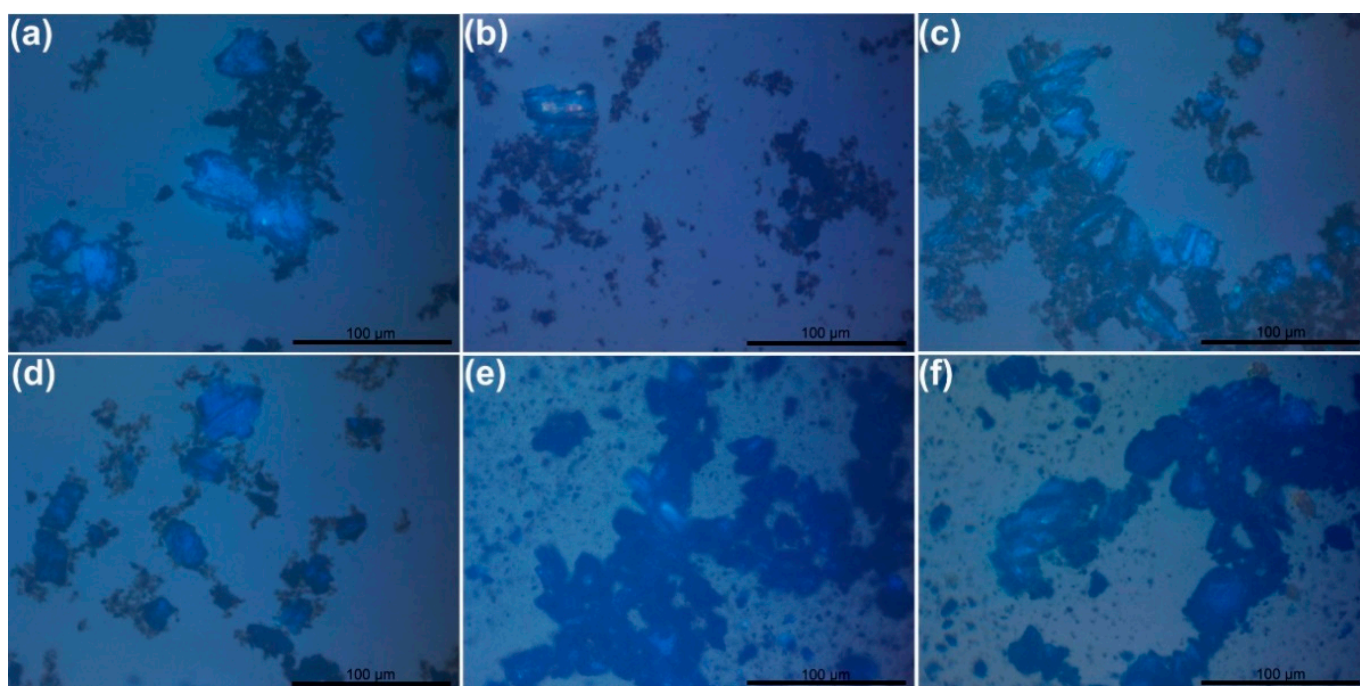


Figure 2. Optical micrographs of GBS obtained after 24 h from the start of the synthesis—A000 (a), A100 (b), P000 (c), P100 (d), C000 (e), and C100 (f).

Many stage I and stage II GICs are colored. A rich blue color is observed in optical microscopy pictures both 2 h and 24 h from the start of the synthesis, indicating the formation of stage I GBS [18,19]. The abundance of blue zones is approximately the same and does not depend on the duration of the synthesis. Therefore, we can conclude that the GBS of stage I represented by the formula $C_{24}^+ \cdot HSO_4^- \cdot 2H_2SO_4$ is stable under the synthesis conditions in a medium of conc. H_2SO_4 . We can also note that the GBS of stage I is more likely to form in the central part of larger crystallites, irrespective of the oxidizing agent. Blue areas are commonly surrounded by crystallites of darker color, which vary from black to brown-yellowish tint. These crystallites might be attributed both to non-intercalated graphite and GBS with a lower staging index [19,20]. Single inserts of this color can be detected in the micrographs of all GBS samples. However, the shape and tint of the brown-yellowish inserts of the GBS samples obtained using CrO_3 (Figure 1e,f and Figure 2f) are slightly different: some of them are lighter in color with more expressed yellow tint and more regular shape. Such a difference may occur due to the presence of either orange-yellowish CrO_3 crystals or miscellaneous Cr(VI) compounds [21].

Raman spectroscopy may help reveal the defectiveness of the carbon materials, staging indices, and the amount of stacked graphene sheets in a layered graphene-like material [19,22–24]. Raman spectra of all samples are provided below (Figures 3–5), and data obtained from the analysis are presented in Table 2 and Figure 6.

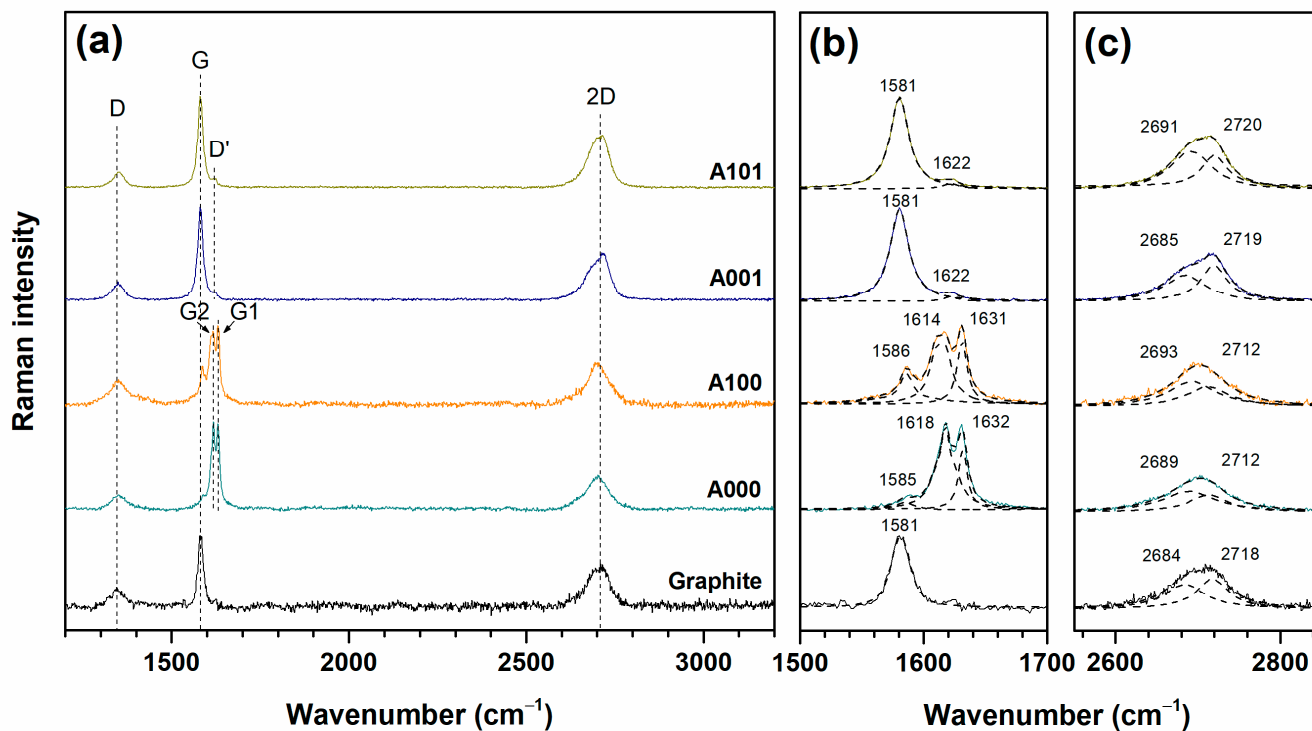


Figure 3. Raman spectra of GBS products obtained using $(\text{NH}_4)_2\text{S}_2\text{O}_8$ oxidizing agent (a), G band frequencies (b), and 2D band frequencies (c).

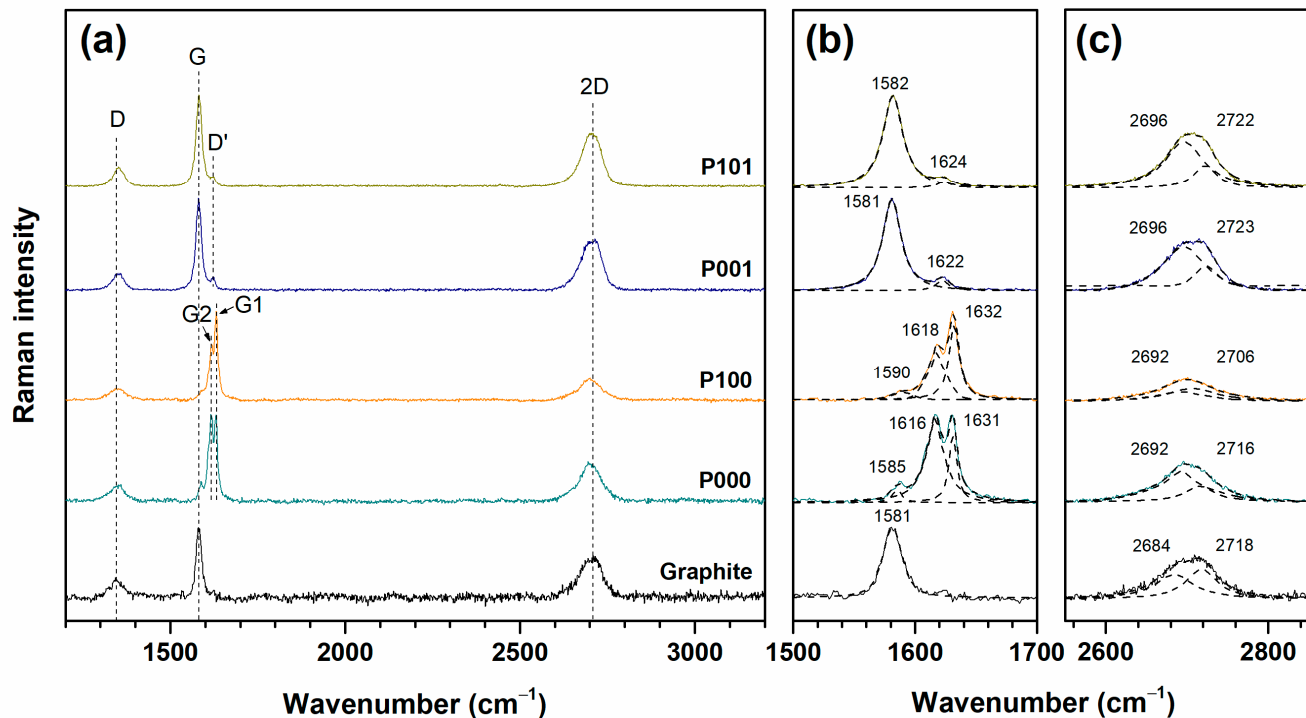


Figure 4. Raman spectra of GBS products obtained using $\text{K}_2\text{S}_2\text{O}_8$ oxidizing agent (a), G band frequencies (b), and 2D band frequencies (c).

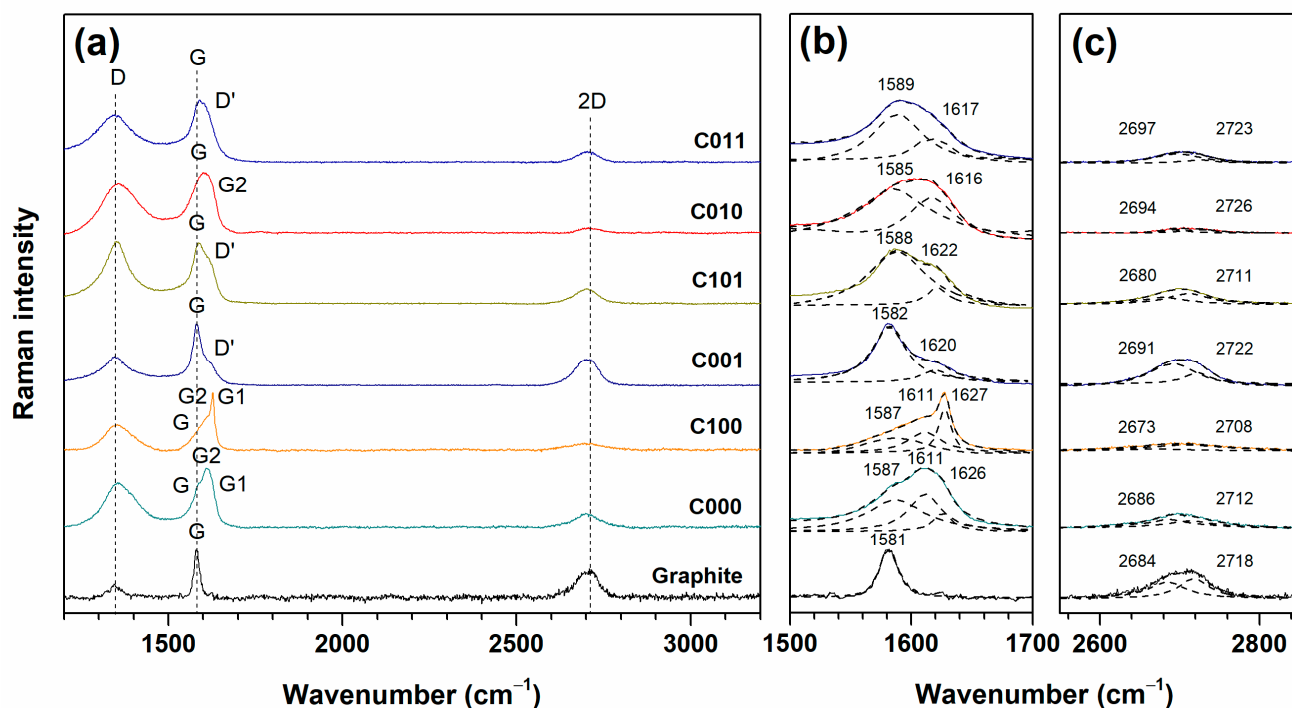


Figure 5. Raman spectra of GBS products obtained using CrO_3 oxidizing agent (a), G band frequencies (b), and 2D band frequencies (c).

Table 2. Amount (%) of stage I, stage II, and non-intercalated graphite phases in GBS samples determined according to the intensities of the G1, G2, and G peaks, respectively.

Sample	Stage I (%)	Stage II (%)	Non-Intercalated Graphite (%)
A000	45.62	46.78	7.60
A100	40.96	38.79	20.25
P000	44.28	45.47	10.25
P100	56.60	37.14	6.26
C000	30.15	31.81	30.05
C100	50.85	29.34	19.81
C010	—	49.63	50.37

Three prominent bands were observed in the resonance Raman spectra of graphite. The D band at 1345 cm^{-1} is caused by defects of the graphene layer (A_{1g} symmetry mode), the G band at 1581 cm^{-1} is assigned to the first-order scattering of E_{2g} mode arising from the sp^2 bonded carbon, and the 2D band at 2709 cm^{-1} is an overtone of the D mode; however, contrary to the D band, this mode is always Raman-allowed and the presence of defects or disorders is not required for activation of this band in the resonance Raman spectrum [22,23,25–29]. In addition to these peaks, at about 1622 cm^{-1} a low intensity band named D' can be seen in Raman spectra of annealed samples. The D' band is the second Raman-forbidden band, which appears as a shoulder at the high-frequency side of the G peak due to the presence of disorder. The D' band appears when randomly distributed impurities interact with extended graphene phonon modes [30]. However, the main attribute observed in the Raman spectra of GBS products is splitting of the G band (see Figures 3–5). Splitting can occur when charged graphite layers adjacent to the intercalated layers are differentiated from those uncharged next to the empty galleries [31]. The effect of splitting is clearly noticeable using the persulfate oxidizing agents ($(\text{NH}_4)_2\text{S}_2\text{O}_8$ and $\text{K}_2\text{S}_2\text{O}_8$; Figures 3 and 4; samples A000, A100, P000, and P100). Simultaneously, the blue shift occurs when the graphene layers are charged with intercalant molecules [18]. This shift, also accompanied by the splitting of the G band into three peaks, evidences the

process of graphite intercalation [32]. The smaller G bands at approximately 1586 cm^{-1} , which remain in the samples A000, A100, P000, and P100, represent the part of graphite that must have remained non-intercalated [13]. The other two peaks, G1 at about 1632 cm^{-1} and G2 at about 1618 cm^{-1} represent stage I and stage II GBS phases, respectively, present in the samples A000, A100, P000, and P100 [33]. The Raman spectra of G bands of GBS phases obtained using both persulfate oxidizing agents are quite similar (Figures 3b and 4b); more differences can be found between the samples with and without using P_2O_5 additive. Meantime, the Raman spectra of the GBS phases obtained using CrO_3 oxidizing agent (Figure 5) show a significant difference from those obtained using the persulfate oxidizing agents. Splitting of the G band for C000 and C100 is implicit, also different from that in the case of the A000, A100, P000, and P100 samples. The G2 peak at 1611 cm^{-1} can be assigned to the GBS stage II phase, and the peak G1 at about 1626 cm^{-1} indicates the stage I GBS compound. In the spectrum of C010, two peaks may be hidden in the amid G band region. The peak in the lower wavenumbers corresponds to graphite, and the G2 peak at about 1616 cm^{-1} is characteristic of stage II GIC. Moreover, it can be seen that the G peaks of the samples synthesized with CrO_3 are clearly broadened. FWHM(G) (full width at half maximum of the G band) represents the degree of the graphitization of carbon materials, which is the grade to which the carbon atoms form a hexagonal close-packed graphite crystalline structure [28]. Therefore, high FWHM(G) values reveal that the use of CrO_3 oxidizer could result in an almost amorphous structure, the formation of vacancies, sp^3 defects as well as reduction in particle size [34].

A comparison of the intensities of peaks G, G1, and G2, evaluated by the fit procedure, was used as a relative indicator of the quantity of different intercalation phases in the samples [13]. The amount of stage I, stage II phases, and non-intercalated graphite according to the intensities of the G1, G2, and G peaks, respectively, are presented in Table 2. Samples A000, P000, and C000 have the majority of stage II GBS compounds, while the stage I GBS is formed mostly when P_2O_5 is added. The GBS sample obtained using CrO_3 oxidizing agent and water at the end of the reaction (sample C010) shows a different case. In this spectrum, the G1 peak cannot be found, which suggests that the stage I GBS phase was not formed in this compound. For this reason, the value of stage I for C010 is blank in Table 2. However, Raman analysis reveals that stage II phase remains in the sample even after washing it with water. Nevertheless, non-intercalated graphite makes up the majority of this compound. Apparently, the addition of P_2O_5 can help to get a higher proportion of intercalated compound, while the addition of H_2O gives the opposite results. In this work, P_2O_5 was used as a dehydration agent. When dissociation of concentrated sulfuric acid occurs, H_3O^+ ion, which is responsible for the acidity, is obtained. When there is no water present, the dissociation of sulfuric acid proceeds in a different way. In that case, H_3SO_4^+ dominates among ions and it is a much stronger acid than H_3O^+ . This results in a higher oxidation state of graphite. For this reason, the addition of P_2O_5 and dehydration can help to reach a higher oxidation state of graphite and, therefore, a higher degree of intercalation [35].

The D band is present in Raman spectra of graphite, all GBS samples, and their annealed products (Figures 3–5). Although the $I(\text{D})/I(\text{G})$ ratio is the most commonly used Raman marker to evaluate the concentration of defects in graphite and graphene-like materials, the splitting of the G band due to the presence of intercalated phases raises the question of whether this ratio can be directly applied as a defect marker. Furthermore, a parameter named FWHM(D) (full width at half maximum of the band D) shows high sensitivity to all types of defects [36]. We used both parameters to evaluate the concentration of defects in the GBS products and to assess the correlation between them (Figure 6a). For $I(\text{D})/I(\text{G})$ calculation, the maximum peak at the G band was normalized to be 1 in an arbitrary unit scale. As one can see in Figure 6a, a positive correlation exists between these two parameters: the higher $I(\text{D})/I(\text{G})$ ratio, as well as the wider FWHM(D), results in a higher concentration of defects. In the correlation chart, a sample C101 stands out; the R^2 value including C101 reaches 0.6256. After excluding C101 from the correlation data set, R^2

risers to 0.8598. The Raman spectrum of C101 is rather different from the other spectra of that series; the D peak is extremely high, and the G band includes a pronounced shoulder of the D' peak. Since the D' peak appears as a result of defects that are different from those caused by the broadening of the D band [36], the high concentration of specific defects may be the reason for non-fitting of the C101 sample to the correlation data set. Figure 6a also shows that the concentration of defects in GBS products obtained using ammonium and potassium persulfate oxidizing agents is much lower compared to those obtained using CrO_3 . Meanwhile, no significant differences can be detected between these two persulfate oxidizing agents. Similar results were obtained by measuring the correlation between the FWHM of two main bands in the Raman spectra of GBS products: FWHM(D) and FWHM(G) (see Figure 6b). While the higher values of both FWHM(D) and FWHM(G) mean the higher defect concentration, two characteristic zones, one for the samples oxidized with CrO_3 and another for the samples oxidized with $(\text{NH}_4)_2\text{S}_2\text{O}_8$ and $\text{K}_2\text{S}_2\text{O}_8$, can be distinguished in the correlation chart. As in the previous case, no significant differences were observed between the action of $(\text{NH}_4)_2\text{S}_2\text{O}_8$ and $\text{K}_2\text{S}_2\text{O}_8$.

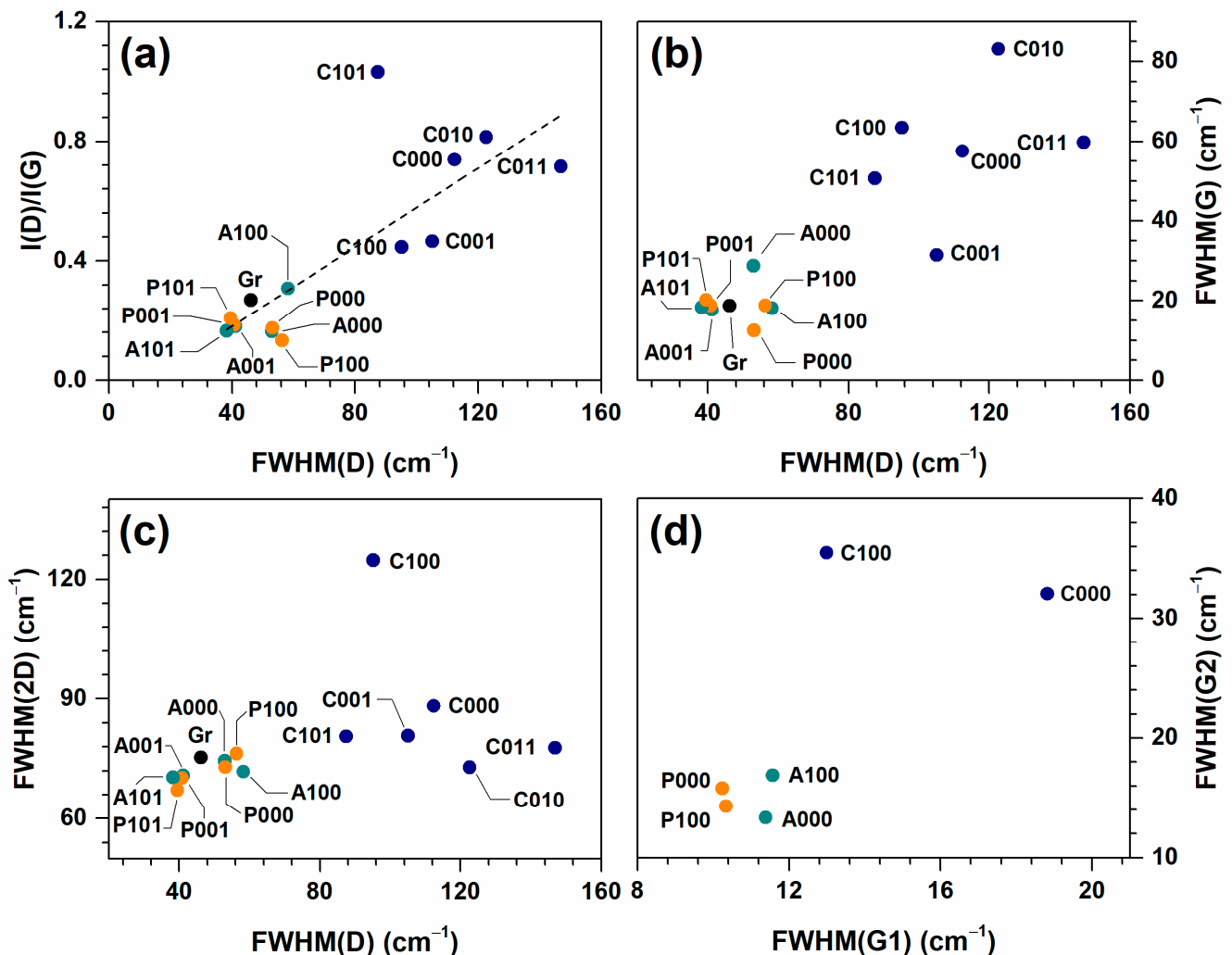


Figure 6. Correlation between FWHM data of Raman spectra of GBS products obtained using different oxidizing agents: FWHM(D) and I(D)/I(G) ratio representing defect concentration in GBS products (a), FWHM(D) and FWHM(G) representing defect and sp^2 bonded carbon vibrations (b), FWHM(D) and FWHM(2D) representing defect and second mode defect vibrations (c), FWHM(G1) and FWHM(G2) representing the staging index (stage I and stage II) (d).

Another important Raman marker is the FWHM(2D) (full width at half maximum of the 2D band), which is frequently used to identify the amount of graphene layers [27]. Single layer graphene has FWHM(2D) values around 30 cm^{-1} . When the number of layers increases, the FWHM values also show an increase [33]. In addition to this, the 2D Raman band shape also helps to distinguish single and bilayer graphene from the multilayer. Monolayer graphene has a single 2D component, bilayer graphene is fitted to four components, and the 2D mode in bulk graphite can be decomposed into two components. In this work, calculated FWHM(2D) values of all samples exceed 60 cm^{-1} and can be best fitted with two components (see Figures 3c, 4c and 5c). Thus, it can be concluded that the materials obtained feature a multilayer structure. The correlation between FWHM(D) and FWHM(2D) shows the presence of two zones, as in previous cases: one for the samples oxidized with CrO_3 , another—for the samples oxidized with persulfates (Figure 6c).

Previously discussed correlations between the parameters in Raman spectra of GBS products do not allow us to distinguish any significant difference between the action of $(\text{NH}_4)_2\text{S}_2\text{O}_8$ and $\text{K}_2\text{S}_2\text{O}_8$. Such a result can be treated as an evident outcome, since the samples in the correlation set include completely different compounds (e.g., intercalates and annealed graphene-like phases). We tried to narrow the correlation set and compared the features of the Raman spectra of intercalated GBS phases (see Figure 6d). By comparing the FWHM(G1) and FWHM(G2), which are sensitive to the presence of defects in the corresponding GBS phase (stage I and stage II correspondingly), one can see that the quality of the phase is extremely sensitive to the use of CrO_3 —it results in the evident increase of defect concentration [36]. Meanwhile, the minimal defect concentration in GBS phases can be reached by using $\text{K}_2\text{S}_2\text{O}_8$, while the use of $(\text{NH}_4)_2\text{S}_2\text{O}_8$ causes a slightly higher concentration of defects. Supposedly, the effect of NH_4^+ ion may be related to its higher redox activity in comparison with the K^+ ion, which is significant in the reaction of carbocation formation (see Equation (1)).

FTIR spectra were employed to determine the functional groups that emerged on the surface of the GBS products obtained using three oxidizing agents: $(\text{NH}_4)_2\text{S}_2\text{O}_8$ (Figure 7), $\text{K}_2\text{S}_2\text{O}_8$ (Figure 8), and CrO_3 (Figure 9). Additionally, the spectrum of the graphite precursor is presented (Figure 7), where the low intensity of the peaks represents a low concentration of surface functional groups in pristine graphite. The most characteristic features are the following: the absorption band at 3435 cm^{-1} (stretching vibrations of the O–H bond), band at 1637 cm^{-1} (stretching vibrations of the C=C bond), and peak at 1418 cm^{-1} (deformation vibrations of the C–OH bond) [28,37]. The addition of an oxidant increases both the intensity and variety of peaks in the FTIR spectra. Some newly appeared peaks may correspond to the SO_2 asymmetric stretching vibrations (1293 cm^{-1}) and S=O (1070 cm^{-1}) groups [13,38]. Peaks at 1231 cm^{-1} and 1167 cm^{-1} may be related to C–O vibrations [28,39,40]; the peak at 1004 cm^{-1} can be assigned to graphitic domains C–O vibrations [41,42], while 882 cm^{-1} and 850 cm^{-1} may correspond to out-of-plane vibrations of the C–H bond [42]. The broad feature in the vicinity of $2700\text{--}3100\text{ cm}^{-1}$ might be related to O–H stretching vibrations of strongly hydrogen-bonded carboxylate groups or adsorbed water molecules and C–H stretching motions [27]. In addition to these bands, the peak at 1117 cm^{-1} (asymmetric SO_4^{2-} vibrations) appears in the FTIR spectrum of the P001 sample [43]. In the spectra of GBS products obtained using CrO_3 (C010 and C011), minor bands that indicate the vibrations in the Cr=O group (950 cm^{-1} and 914 cm^{-1}), are also introduced [44]. After thermal treatment, absorption bands related to oxygen-containing groups in the fingerprint area mostly disappear, though a band in the vicinity of about 1070 cm^{-1} , which indicates the presence of S=O group, remains. As can be seen, during the intercalation of graphite, some of the carbon double bonds can be oxidized by strong acids, leading to the formation of oxygen-containing functional groups, and sulfur derivatives can be intercalated into the graphite structure [45]. In addition, analysis showed that the functional groups introduced during the intercalation process were not influenced using different persulfate oxidizing

agents; however, using CrO_3 oxidizer determined that a small part of $\text{Cr}=\text{O}$ groups was formed during the synthesis reaction.

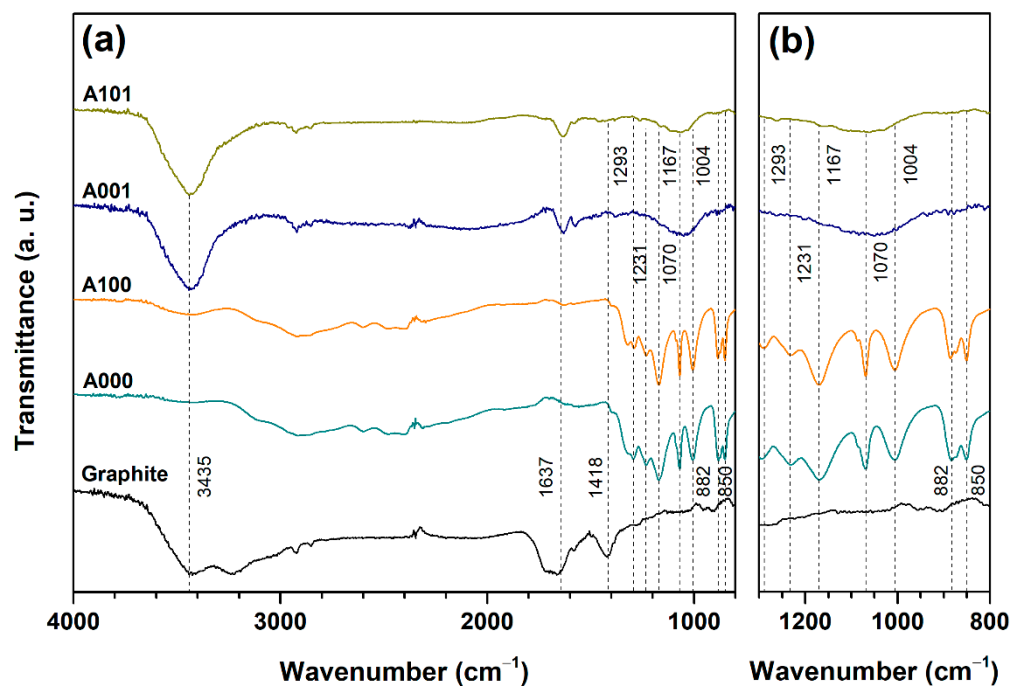


Figure 7. FTIR spectra of GBS products obtained using $(\text{NH}_4)_2\text{S}_2\text{O}_8$ oxidizing agent in the region of $4000\text{--}800\text{ cm}^{-1}$ (a) and $1300\text{--}800\text{ cm}^{-1}$ (b).

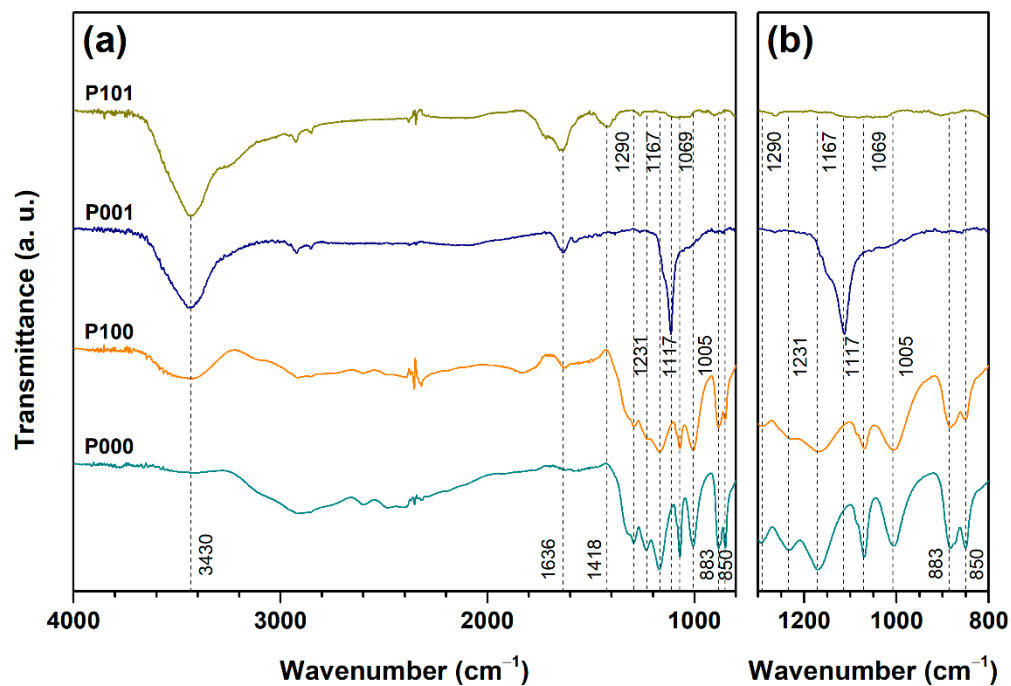


Figure 8. FTIR spectra of GBS products obtained using $\text{K}_2\text{S}_2\text{O}_8$ oxidizing agent in the region of $4000\text{--}800\text{ cm}^{-1}$ (a) and $1300\text{--}800\text{ cm}^{-1}$ (b).

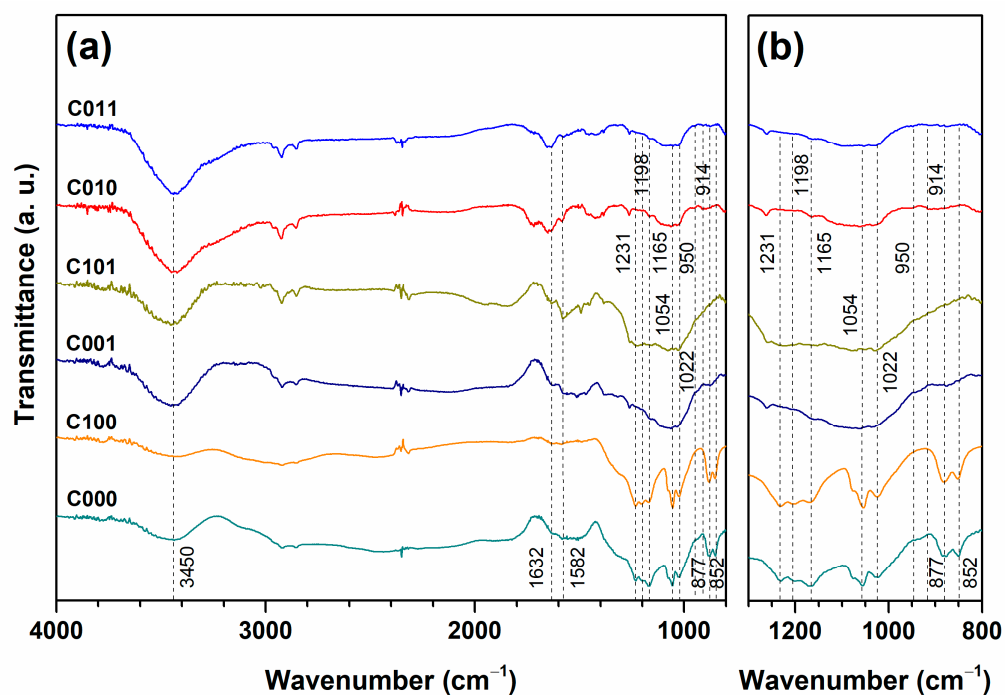


Figure 9. FTIR spectra of GBS products obtained using Cr_2O_3 oxidizing agent in the region of $4000\text{--}800\text{ cm}^{-1}$ (a) and $1300\text{--}800\text{ cm}^{-1}$ (b).

The annealed GBS products, together with the GBS sample washed with H_2O (C010), were examined using XRD analysis. The XRD patterns are presented in Figure 10. The XRD pattern of pristine graphite is also presented for comparison. The determined values of interplanar spacing d_{002} and crystallite size L are presented in Table 3.

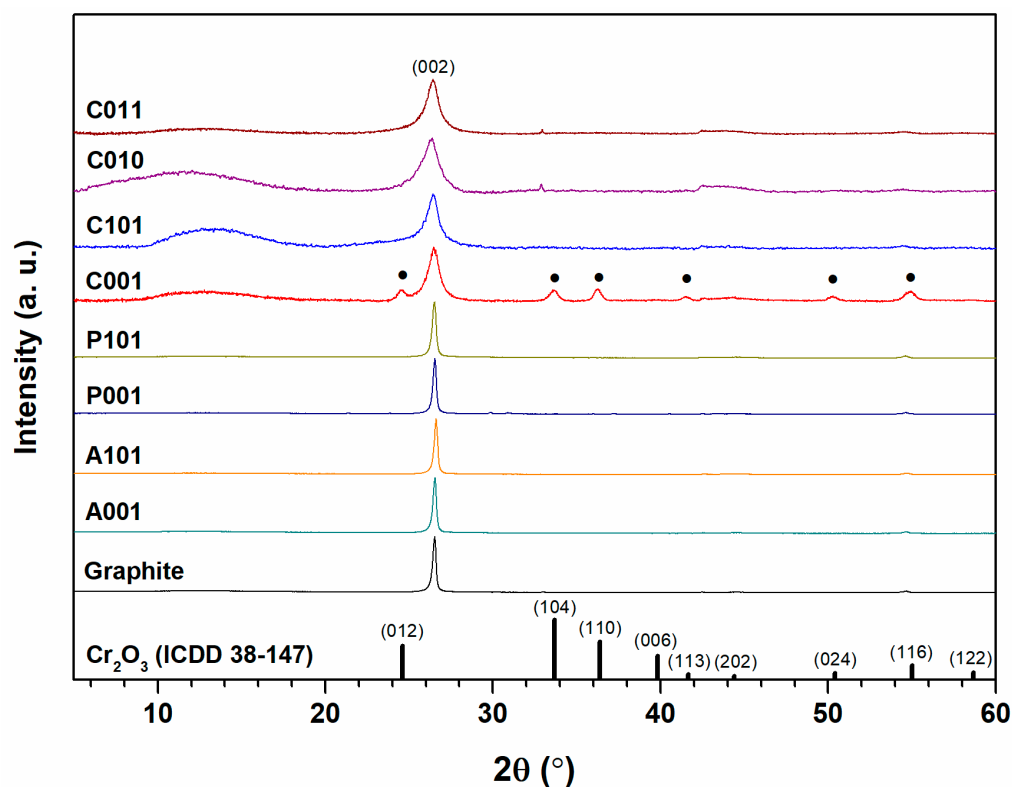


Figure 10. XRD patterns of GBS products, graphite, and Cr_2O_3 (ICDD 38-147; marked with •).

Table 3. XRD peak positions, interplanar spacing d_{002} and crystallite size of the annealed and water-treated GBS products.

Sample	2θ (deg)	d_{002} (nm)	L (nm)
Graphite	26.53	0.335	27.87
A001	26.55	0.335	27.40
P001	26.54	0.335	27.58
C001	26.48	0.336	7.34
A101	26.61	0.334	27.37
P101	26.52	0.335	23.71
C101	26.41	0.337	4.49
C010	26.41	0.337	4.36
C011	26.43	0.337	5.87

The use of $(\text{NH}_4)_2\text{S}_2\text{O}_8$ and $\text{K}_2\text{S}_2\text{O}_8$ oxidizing agents made it possible to obtain GBS products which, after annealing, return to the graphite-like structure: the peak positions, crystallite sizes and interplanar spacing of A001, A101, P001, and P101 closely coincide with that of pristine graphite (Table 3). Different results were obtained using the CrO_3 oxidizing agent. The peak (002) is clearly broadened compared to that of pure graphite. This is most likely caused by the drastic decrease in average particle size. As in most cases, smaller particles lead to broader reflections as estimated by the Scherrer equation. Such a result is observed not only for the annealed GBS products, but also for sample C010, which is obtained by adding water at the end of the intercalation reaction. A broadened peak with the maximum position at about 11.5° in the XRD pattern of the C010 sample supposedly indicates the presence of the structure, which is similar to that of graphite oxide. Furthermore, compared to the graphite, the (002) peak is shifted to lower 2θ angles and the interplanar spacing is increased from 0.335 nm up to 0.337 nm in GBS products obtained with CrO_3 . A shift to lower angles can occur due to the presence of defects in the crystal lattice [13]. This observation, together with the Raman analysis, indicates that the GBS produced with CrO_3 can have a significant number of defects. Additional peaks (marked with dots) were also observed in the XRD patterns, where CrO_3 was used. These peaks may indicate the presence of Cr_2O_3 . This compound can be formed when CrO_3 remains in the mixture and decomposes into Cr_2O_3 during thermal treatment [46]. The Cr_2O_3 reference pattern (ICDD 38-147) is shown in Figure 10 for comparison.

SEM micrographs were used to assess the surface morphology of the annealed GBS samples and compare it to that of pristine graphite (Figure 11).

The variable surface morphology of GBS products is evident. The SEM image of the pristine graphite sample (Figure 11a) revealed the presence of lamellar structure and flat surfaces with regular edges. The use of $(\text{NH}_4)_2\text{S}_2\text{O}_8$ and $\text{K}_2\text{S}_2\text{O}_8$ oxidizing agents produces particles with an expanded lamellar structure and less regular edges (Figure 11b–e). Significant differences in the morphology of GBS products appear after the use of CrO_3 oxidizing agent (Figure 11f–i); the lamellar structure becomes much less pronounced, while the edges of the particles turn highly jagged and irregular. This observation is in good agreement with the results discussed previously, as the use of CrO_3 in the GBS synthesis results in the most affected graphite structure.

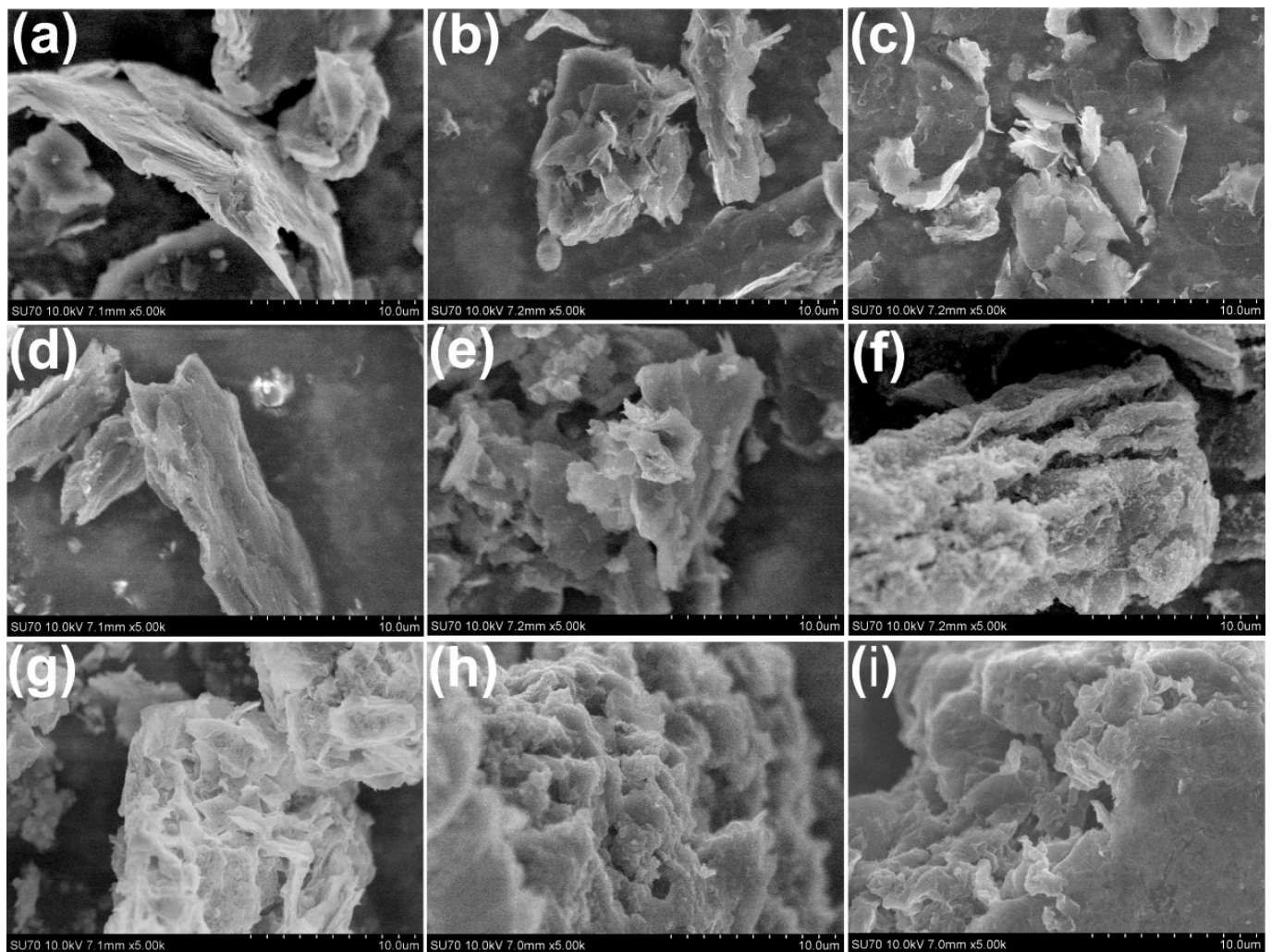


Figure 11. SEM micrographs of pristine graphite and GBS products: graphite (a), A001 (b), A101 (c), P001 (d), P101 (e), C001 (f), C101 (g), C010 (h), and C011 (i).

4. Conclusions

In this work, samples of GBS were synthesized using three different oxidizing agents: $(\text{NH}_4)_2\text{S}_2\text{O}_8$, $\text{K}_2\text{S}_2\text{O}_8$, and CrO_3 with and without using P_2O_5 as the water-binding agent. In addition, all the specimens obtained were heat-treated at 800°C . Optical microscopy pictures taken after 2 and 24 h from the start of the synthesis show blue GBS particles, which correspond to stage I of the GBS compound, confirming that graphite has been successfully intercalated and is stable under used synthesis conditions in a medium of conc. H_2SO_4 . Raman spectroscopy analysis revealed differences between the GBS phases and annealed GBS products when using all three oxidizing agents and P_2O_5 . It was established that when P_2O_5 acts as a dehydration agent, the intercalation system can reach a higher acidity, resulting in a higher oxidation state of graphite and a more effective intercalation. Correlation between different characteristic parameters of the Raman analysis has shown that the use of CrO_3 results in a much higher defect concentration compared to the GBS products obtained using persulfate oxidizers. The correlation among all GBS products did not allow us to distinguish any significant difference between the action of $(\text{NH}_4)_2\text{S}_2\text{O}_8$ and $\text{K}_2\text{S}_2\text{O}_8$. However, narrowing the correlation set only to the characteristic parameters of GBS phases (stage I and stage II) revealed that the difference between the action of $\text{K}_2\text{S}_2\text{O}_8$ and $(\text{NH}_4)_2\text{S}_2\text{O}_8$ is still noticeable. The minimal defect concentration in the GBS phases can be reached by using $\text{K}_2\text{S}_2\text{O}_8$, while the use of $(\text{NH}_4)_2\text{S}_2\text{O}_8$ causes a slightly higher concentration of defects. Supposedly, the effect of the NH_4^+ ion may be related to

its higher redox activity in comparison with the K^+ ion, which is significant in the reaction of carbocation formation. FTIR analysis has shown that during graphite intercalation, part of the carbon double bonds is oxidized, and sulfur derivatives are intercalated into the graphite structure. XRD analysis revealed that after heat treatment, GBS products mostly returned to a graphite-like structure; however, several differences were observed in samples with CrO_3 . These compounds are characterized by the largest interplanar distances and the smallest crystallite sizes. SEM pictures confirm that the most significant changes in surface morphology were observed in the GBS products obtained using the CrO_3 oxidizing agent.

Author Contributions: Conceptualization, G.R., M.G., J.B., A.Z., J.G. and G.N.; methodology, J.B., J.G. and G.N.; formal analysis, J.B. and G.R.; investigation, M.G. and G.R.; resources, J.B. and J.G.; data curation, G.R., M.G., J.B., J.G. and G.N.; writing—original draft preparation, G.R.; writing—review and editing, G.R., M.G., J.B., A.Z., J.G. and G.N.; supervision, J.B. and J.G. All authors have read and agreed to the published version of the manuscript.

Funding: This research received no external funding.

Institutional Review Board Statement: Not applicable.

Informed Consent Statement: Not applicable.

Data Availability Statement: Data are contained within the article.

Conflicts of Interest: The authors declare no conflict of interest.

References

1. Schafhaeutl, C. Ueber Die Verbindungen Des Kohlenstoffes Mit Silicium, Eisen Und Anderen Metallen, Welche Die Verschiedenen Gallungen von Roheisen, Stahl Und Schmiedeeisen Bilden. *J. Prakt. Chem.* **1840**, *21*, 129–157. [[CrossRef](#)]
2. Brodie, B. Note Sur Un Nouveau Procédé Pour La Purification et La Désagrégation Du Graphite. *Ann. Chim. Phys.* **1855**, *45*, 351–353.
3. Brédas, J.-L.; Buriak, J.M.; Caruso, F.; Choi, K.-S.; Korgel, B.A.; Palacín, M.R.; Persson, K.; Reichmanis, E.; Schüth, F.; Seshadri, R.; et al. An Electrifying Choice for the 2019 Chemistry Nobel Prize: Goodenough, Whittingham, and Yoshino. *Chem. Mater.* **2019**, *31*, 8577–8581. [[CrossRef](#)]
4. Li, Y.; Lu, Y.; Adelmhelm, P.; Titirici, M.-M.; Hu, Y.-S. Intercalation Chemistry of Graphite: Alkali Metal Ions and Beyond. *Chem. Soc. Rev.* **2019**, *48*, 4655–4687. [[CrossRef](#)]
5. Xu, J.; Dou, Y.; Wei, Z.; Ma, J.; Deng, Y.; Li, Y.; Liu, H.; Dou, S. Recent Progress in Graphite Intercalation Compounds for Rechargeable Metal (Li, Na, K, Al)-Ion Batteries. *Adv. Sci.* **2017**, *4*, 1700146. [[CrossRef](#)] [[PubMed](#)]
6. Setton, R.; Beguin, F.; Piroelle, S. Graphite Intercalation Compounds as Reagents in Organic Synthesis. An Overview and Some Recent Applications. *Synth. Met.* **1982**, *4*, 299–318. [[CrossRef](#)]
7. Smith, R.P.; Weller, T.E.; Howard, C.A.; Dean, M.P.M.; Rahnejat, K.C.; Saxena, S.S.; Ellerby, M. Superconductivity in Graphite Intercalation Compounds. *Phys. C Supercond. Its Appl.* **2015**, *514*, 50–58. [[CrossRef](#)]
8. Abdelkader, A.M.; Cooper, A.J.; Dryfe, R.A.W.; Kinloch, I.A. How to Get between the Sheets: A Review of Recent Works on the Electrochemical Exfoliation of Graphene Materials from Bulk Graphite. *Nanoscale* **2015**, *7*, 6944–6956. [[CrossRef](#)]
9. Li, C.; Shi, Y.; Chen, X.; He, D.; Shen, L.; Bao, N. Controlled Synthesis of Graphite Oxide: Formation Process, Oxidation Kinetics, and Optimized Conditions. *Chem. Eng. Sci.* **2018**, *176*, 319–328. [[CrossRef](#)]
10. Sorokina, N.E.; Nikol'skaya, I.V.; Ionov, S.G.; Avdeev, V.V. Acceptor-Type Graphite Intercalation Compounds and New Carbon Materials Based on Them. *Russ. Chem. Bull.* **2005**, *54*, 1749–1767. [[CrossRef](#)]
11. Bonaccorso, F.; Lombardo, A.; Hasan, T.; Sun, Z.; Colombo, L.; Ferrari, A.C. Production and Processing of Graphene and 2d Crystals. *Mater. Today* **2012**, *15*, 564–589. [[CrossRef](#)]
12. Chung, D.D.L. A Review of Exfoliated Graphite. *J. Mater. Sci.* **2015**, *51*, 554–568. [[CrossRef](#)]
13. Salvatore, M.; Carotenuto, G.; de Nicola, S.; Camerlingo, C.; Ambrogi, V.; Carfagna, C. Synthesis and Characterization of Highly Intercalated Graphite Bisulfate. *Nanoscale Res. Lett.* **2017**, *12*, 167. [[CrossRef](#)]
14. Dimiev, A.M.; Bachilo, S.M.; Saito, R.; Tour, J.M. Reversible Formation of Ammonium Persulfate/Sulfuric Acid Graphite Intercalation Compounds and Their Peculiar Raman Spectra. *ACS Nano* **2012**, *6*, 7842–7849. [[CrossRef](#)] [[PubMed](#)]
15. Lünsdorf, N.K. Raman Spectroscopy of Dispersed Vitrinite—Methodical Aspects and Correlation with Reflectance. *Int. J. Coal Geol.* **2016**, *153*, 75–86. [[CrossRef](#)]
16. Zaaba, N.I.; Foo, K.L.; Hashim, U.; Tan, S.J.; Liu, W.W.; Voon, C.H. Synthesis of Graphene Oxide Using Modified Hummers Method: Solvent Influence. *Procedia Eng.* **2017**, *184*, 469–477. [[CrossRef](#)]
17. Ivanov, A.V.; Maksimova, N.V.; Kamaev, A.O.; Malakho, A.P.; Avdeev, V.V. Influence of Intercalation and Exfoliation Conditions on Macrostructure and Microstructure of Exfoliated Graphite. *Mater. Lett.* **2018**, *228*, 403–406. [[CrossRef](#)]

18. Dimiev, A.M.; Shukhina, K.; Behabtu, N.; Pasquali, M.; Tour, J.M. Stage Transitions in Graphite Intercalation Compounds: Role of the Graphite Structure. *J. Phys. Chem. C* **2019**, *123*, 19246–19253. [[CrossRef](#)]
19. Seiler, S.; Halbig, C.E.; Grote, F.; Rietsch, P.; Börrnert, F.; Kaiser, U.; Meyer, B.; Eigler, S. Effect of Friction on Oxidative Graphite Intercalation and High-Quality Graphene Formation. *Nat. Commun.* **2018**, *9*, 836. [[CrossRef](#)]
20. Dimiev, A.M.; Shukhina, K.; Khannanov, A. Mechanism of the Graphene Oxide Formation. The Role of Water, “Reversibility” of the Oxidation, and Mobility of the C–O Bonds. *Carbon* **2020**, *166*, 1–14. [[CrossRef](#)]
21. 3—Fixation. In *Chromosome Techniques*, 3rd ed.; Sharma, A.K.; Sharma, A. (Eds.) Butterworth-Heinemann: Boston, MA, USA, 1980; pp. 30–70, ISBN 978-0-408-70942-2.
22. Ferrari, A.C.; Robertson, J. Raman Spectroscopy of Amorphous, Nanostructured, Diamond-like Carbon, and Nanodiamond. *Philos. Trans. R. Soc. A Math. Phys. Eng. Sci.* **2004**, *362*, 2477–2512. [[CrossRef](#)] [[PubMed](#)]
23. Trusovas, R.; Ratautas, K.; Račiukaitis, G.; Niaura, G. Graphene Layer Formation in Pinewood by Nanosecond and Picosecond Laser Irradiation. *Appl. Surf. Sci.* **2019**, *471*, 154–161. [[CrossRef](#)]
24. ChacónChac, J.C.; Wirtz, L.; Pichler, T. Raman Spectroscopy of Graphite Intercalation Compounds: Charge Transfer, Strain, and Electron-Phonon Coupling in Graphene Layers. *Phys. Status Solidi B* **2014**, *251*, 2337–2355. [[CrossRef](#)]
25. Gurzęda, B.; Buchwald, T.; Krawczyk, P. Thermal Exfoliation of Electrochemically Synthesized Graphite Intercalation Compound with Perrhenic Acid. *J. Solid State Electrochem.* **2020**, *24*, 1363–1370. [[CrossRef](#)]
26. Eigler, S. Graphite Sulphate—A Precursor to Graphene. *Chem. Commun.* **2015**, *51*, 3162–3165. [[CrossRef](#)] [[PubMed](#)]
27. Pei, S.; Wei, Q.; Huang, K.; Cheng, H.; Ren, W. Green synthesis of graphene oxide by seconds timescale water electrolytic oxidation. *Nat. Commun.* **2018**, *9*, 145. [[CrossRef](#)] [[PubMed](#)]
28. Trusovas, R.; Račiukaitis, G.; Niaura, G.; Barkauskas, J.; Valušis, G.; Pauliukaite, R. Recent Advances in Laser Utilization in the Chemical Modification of Graphene Oxide and Its Applications. *Adv. Opt. Mater.* **2016**, *4*, 37–65. [[CrossRef](#)]
29. Ferrari, A.C. Raman Spectroscopy of Graphene and Graphite: Disorder, Electron-Phonon Coupling, Doping and Nonadiabatic Effects. *Solid State Commun.* **2007**, *143*, 47–57. [[CrossRef](#)]
30. Douda, J.; González Vargas, C.R.; Basiuk, E.V.; Díaz Cano, A.I.; Fuentes García, J.A.; Hernández Contreras, X.A. Optical Properties of Amine-Functionalized Graphene Oxide. *Appl. Nanosci.* **2019**, *9*, 567–578. [[CrossRef](#)]
31. Zou, J.; Sole, C.; Drewett, N.E.; Velický, M.; Hardwick, L.J. In Situ Study of Li Intercalation into Highly Crystalline Graphitic Flakes of Varying Thicknesses. *J. Phys. Chem. Lett.* **2016**, *7*, 4291–4296. [[CrossRef](#)]
32. Zhou, X.; Liu, Q.; Jiang, C.; Ji, B.; Ji, X.; Tang, Y.; Cheng, H.-M. Strategies towards Low-Cost Dual-Ion Batteries with High Performance. *Angew. Chem. Int. Ed.* **2020**, *59*, 3802–3832. [[CrossRef](#)]
33. Dimiev, A.M.; Ceriotti, G.; Behabtu, N.; Zakhidov, D.; Pasquali, M.; Saito, R.; Tour, J.M. Direct Real-Time Monitoring of Stage Transitions in Graphite Intercalation Compounds. *ACS Nano* **2013**, *7*, 2773–2780. [[CrossRef](#)] [[PubMed](#)]
34. Gaidukevic, J.; Aukstakojyte, R.; Navickas, T.; Pauliukaite, R.; Barkauskas, J. A Novel Approach to Prepare Highly Oxidized Graphene Oxide: Structural and Electrochemical Investigations. *Appl. Surf. Sci.* **2021**, *567*, 150883. [[CrossRef](#)]
35. Melezhyk, A.V.; Tkachev, A.G. Synthesis of graphene nanoplatelets from peroxosulfate graphite intercalation compounds. *Наносистемы физика Химия Математика* **2014**, *5*, 294–306.
36. Nagyte, V.; Kelly, D.J.; Felten, A.; Picardi, G.; Shin, Y.Y.; Alieva, A.; Worsley, R.E.; Parvez, K.; Dehm, S.; Krupke, R.; et al. Raman Fingerprints of Graphene Produced by Anodic Electrochemical Exfoliation. *Nano Lett.* **2020**, *20*, 3411–3419. [[CrossRef](#)]
37. Lavin-Lopez, M.P.; Patón-Carrero, A.; Muñoz-García, N.; Enguilo, V.; Valverde, J.L.; Romero, A. The Influence of Graphite Particle Size on the Synthesis of Graphene-Based Materials and Their Adsorption Capacity. *Colloids Surf. A Physicochem. Eng. Asp.* **2019**, *582*, 123935. [[CrossRef](#)]
38. Martínez-Rubi, Y.; Gonzalez-Dominguez, J.M.; Ansón-Casaos, A.; Kingston, C.T.; Daroszewska, M.; Barnes, M.; Hubert, P.; Cattin, C.; Martínez, M.T.; Simard, B. Tailored SWCNT Functionalization Optimized for Compatibility with Epoxy Matrices. *Nanotechnology* **2012**, *23*, 285701. [[CrossRef](#)]
39. Bera, M.; Gupta, P.; Maji, P.K. Facile One-Pot Synthesis of Graphene Oxide by Sonication Assisted Mechanochemical Approach and Its Surface Chemistry. *J. Nanosci. Nanotechnol.* **2018**, *18*, 902–912. [[CrossRef](#)]
40. Țucureanu, V.; Matei, A.; Avram, A.M. FTIR Spectroscopy for Carbon Family Study. *Crit. Rev. Anal. Chem.* **2016**, *46*, 502–520. [[CrossRef](#)]
41. Zhong, L.; Yun, K. Graphene Oxide—Modified ZnO Particles: Synthesis, Characterization and Application. *Int. J. Nanomed.* **2018**, *10*, 79–92.
42. He, X.; Liu, X.; Nie, B.; Song, D. FTIR and Raman Spectroscopy Characterization of Functional Groups in Various Rank Coals. *Fuel* **2017**, *206*, 555–563. [[CrossRef](#)]
43. Kusriani, E.; Ng, S.S.; Yulizar, Y.; Ismail, D. Effects of Monocarboxylic Acids and Potassium Persulfate on Preparation of Chitosan Nanoparticles. *Int. J. Technol.* **2015**, *6*, 10–21. [[CrossRef](#)]
44. Trivedi, M.K. Characterization of Physical, Thermal and Structural Properties of Chromium (VI) Oxide Powder: Impact of Biofield Treatment. *J. Powder Metall. Min.* **2015**, *4*, 128. [[CrossRef](#)]
45. Konwer, S.; Gogoi, J.P.; Kalita, A.; Dolui, S.K. Synthesis of Expanded Graphite Filled Polyaniline Composites and Evaluation of Their Electrical and Electrochemical Properties. *J. Mater. Sci. Mater. Electron.* **2011**, *22*, 1154–1161. [[CrossRef](#)]
46. Sajadi, S.A.A.; Khaleghian, M. Study of Thermal Behavior of CrO₃ Using TG and DSC. *J. Therm. Anal. Calorim.* **2014**, *116*, 915–921. [[CrossRef](#)]